Torsional Oscillation Damping Analysis and Suppression Strategy for PMSG-based Wind Generation System

Yizhuo Ma, *Graduate Student Member*, *IEEE*, Jin Xu, Guojie Li, *Senior Member*, *IEEE*, and Keyou Wang, *Member*, *IEEE*

***Abstract*—External disturbances can induce torsional oscillation with weak damping in the shaft system of permanent magnet synchronous generators (PMSGs) based wind generation system, thereby inducing low-frequency oscillations. However, the influence of electromagnetic torque on the shaft system damping and corresponding parameter laws have been scarcely explored. We define the electrical damping coefficient as a quantitative measure for the influence of electromagnetic torque on the shaft system damping. The torsional oscillation damping characteristics of the shaft system under vector control are analyzed, and the transfer function for electromagnetic torque and speed is derived. Additionally, we elucidate the mechanism by which the electromagnetic torque influences the shaft system damping. Simultaneously, laws describing the influence of wind speed, system parameters, and control parameters on the torsional oscillation damping are analyzed. Accordingly, the optimal damping angle of the shaft system a torsional oscillation suppression strategy is proposed to compensate for with uncertainty in the parameters affecting damping. The studied system is modeled using MATLAB/Simulink, and the simulation results validate the effectiveness of the theoretical analysis and proposed torsional oscillation suppression strategy.**

***Index Terms*—Permanent magnet synchronous generator (PMSG), wind generation system, torsional oscillation, shaft system model, damping, oscillation suppression.**

I. Introduction

MANY countries have recently established carbon neutrality targets. In line with these targets, the installed wind power capacity is projected to grow by 430 GW from 2022 to 2025, reflecting an upward trend in wind power adoption [1], [2]. The permanent magnet synchronous generator (PMSG) based wind generation system has gained popularity owing to benefits such as gearbox-free operation and high energy conversion efficiency and performance [3], [4]. The integration of large-scale grid-connected wind power systems poses various challenges to power systems, including power quality, voltage and frequency control, security, and stability [5]. Therefore, the dynamic characteristics of PMSG-based wind generation systems must be examined along with their interactions with power grids [6]. Furthermore, analyzing and understanding the dynamic characteristics of the shaft system in PMSG-based wind generation systems can notably enhance the safe and stable operation of power systems [7].

Compared with the doubly-fed induction generator, the shaft system of PMSG is simpler and consists of only three main components: wind turbine (WT), low-speed transmission shaft, and generator. These components are directly connected without a gearbox through a low-speed transmission [8], [9]. Owing to its multipole structure, the shaft system of PMSG is more flexible than that in a conventional power plant [10]. In addition, the PMSG has more pole pairs in addition to the flexible shaft system [11].

Although a single-mass model may explain the transient instability in a PMSG under drastic disturbances, a double-mass model is required to accurately represent the system dynamics [12]. This is because the double-mass model accurately represents the flexibility and mechanical oscillations of the shaft system.

Under severe external disturbances such as short-circuit faults, the shaft system in a PMSG-based wind generation system experiences torsional oscillation, resulting in power oscillation in the grid-connected wind power system [11]. Torsional oscillations not only induce fatigue in the transmission shaft, thereby reducing its service life, but also give rise to low-frequency oscillations, potentially compromising the safety and stability of the entire PMSG-based wind generation systems [12]. Hence, the torsional oscillations in PMSG-based wind generation systems must be investigated [13].

The torsional oscillation characteristics of PMSG-based wind generation systems are influenced by three factors: input mechanical torque, inherent torque of the shaft system, and input electromagnetic torque under external disturbances [14]. The former two factors are determined by the intrinsic system characteristics, including the generator rotor [15].

Manuscript received: February 29, 2024; revised: April 1, 2024; accepted: May 22, 2024. Date of CrossCheck: May 22, 2024. Date of online publication: July 5, 2024.

This work was supported in part by the National Key R&D Program of China (No. 2022YFE0105200) and in part by State Grid Zhejiang Electric Power Company Science and Technology Program (No. 5211JX230004).

Y. Ma, J. Xu (corresponding author), G. Li, and K. Wang are with the Key Laboratory of Control of Power Transmission and Conversion Ministry of Education, Shanghai Jiao Tong University, Shanghai 200240, China (e-mail: 925998709@sjtu.edu.cn; xujin20506@sjtu.edu.cn; liguojie@sjtu.edu.cn; wangkeyou@sjtu.edu.cn).

DOI: 10.35833/MPCE.2024.000219

The effect of the electromagnetic torque on the torsional oscillation and its potential for oscillation suppression have been analyzed in [16] and [17]. However, a research gap persists concerning the specific parameters and underlying laws that govern the influence of the electromagnetic torque on torsional oscillation characteristics. Therefore, the damping characteristics of PMSG transmission shafting should be unveiled, and its influence mechanism should be understood. This study provides insights into the torsional oscillation characteristics of PMSG-based wind generation systems. Bridging this research gap may have practical implications for designing and optimizing torsional oscillation damping controllers.

To enhance the stability of PMSG-based wind generation systems, various active damping control methods have been devised to mitigate torsional oscillation [18]-[20]. In [18], a simple real power control strategy is introduced based on the rapid torque control for a direct-drive wind energy conversion system employing a PMSG. This study also outlines the parameter tuning procedure for the proposed control strategy. In [19], a sensorless active damping control strategy for direct-driven permanent magnet WT generators uses cascade observers to estimate the speeds of the WT and PMSG. In [20], the torsional oscillation damping is improved by adding a damping transfer function proportional to the speed difference between the WT and generator. Although previous studies have suggested methods to suppress torsional oscillations, to the best of our knowledge, few of them have thoroughly and quantitatively analyzed the mechanism of the influence of electromagnetic torque on the shaft system damping. In addition, an optimal damping angle compensation method has not been devised to improve the system stability.

We analyze the torsional oscillation damping characteristics under vector control using an electromagnetic damping torque method. The electrical damping coefficient is defined as a quantitative representation of the effect of the electromagnetic torque on the shaft system damping. Then, the transfer function for electromagnetic torque and speed is derived, and the influence of the electromagnetic torque on the shaft system damping is characterized. Further, the impact of wind speed, system parameters, and control parameters on torsional oscillation damping are examined in detail. Based on these findings, we propose a torsional oscillation suppression strategy for the active power control section of a machine-side converter (MSC). This strategy compensates for the damping angle of the shaft system and ensures the maximum damping.

II. Modeling and Control of PMSG-based Wind Generation System

The topology of a grid-connected PMSG-based wind generation system typically includes the shaft system, PMSG, back-to-back full-power converter, transformers, and the control sections of the grid-side converter (GSC) and MSC, as shown in Fig. 1, where MPPT is short for maximum power point tracking; PI is short for proportional and integral; PCC is short for point of common coupling; and PLL is short for phase-locked loop. This section presents a mathematical model of the considered system using the per-unit system.

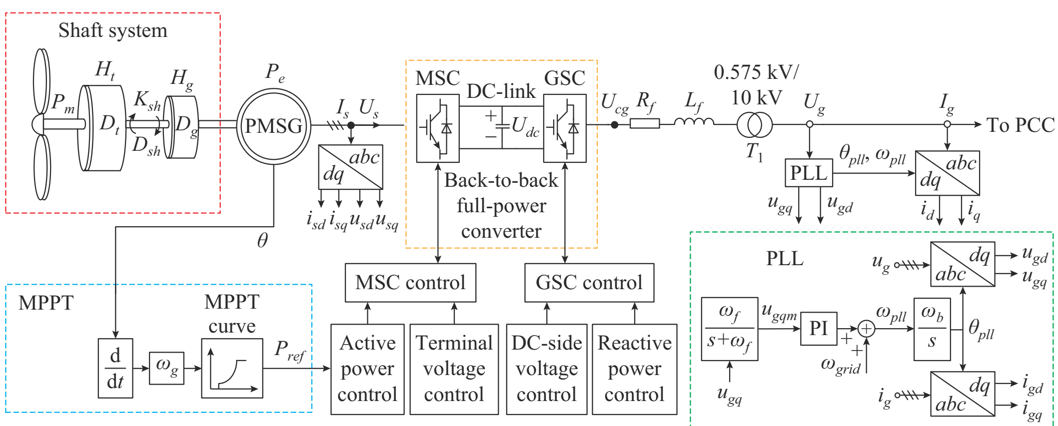

Fig. 1. Typical topology of PMSG-based wind generation system.

A. PMSG Model

The PMSG is controlled in the d-q rotating coordinates with the d-axis aligned with magnetic flux linkage of PMSG rotor ψ_f. The stator voltage of PMSG is given by [21]:

$$\begin{cases} u_{sd}=-R_s i_{sd}-\dfrac{L_d}{\omega_{eb}}\dfrac{\mathrm{d}i_{sd}}{\mathrm{d}t}+\omega_g L_q i_{sq} \\ u_{sq}=-R_s i_{sq}-\dfrac{L_d}{\omega_{eb}}\dfrac{\mathrm{d}i_{sq}}{\mathrm{d}t}-\omega_g L_d i_{sd}+\omega_g \psi_f \end{cases} \tag{1}$$

where u_{sd} and u_{sq} are the d- and q-axis stator terminal voltages, respectively; i_{sd} and i_{sq} are the d- and q-axis stator currents, respectively; R_s is the stator resistance of PMSG; ω_{eb} is the base value of stator angular frequency; ω_g is the angular frequency of PMSG rotor; and L_d and L_q are the d- and q-axis self-inductances of PMSG stator, respectively.

The speed of a megawatt PMSG is relatively low, and most PMSG is nonsalient surface-mounted ($L_d=L_q$). Therefore, the electromagnetic torque T_e can be formulated as [20]:

$$T_e=\psi_f i_{sq} \tag{2}$$

B. Double-mass Model

The double-mass model can be expressed as [16]:

$$\begin{cases} 2H_t \dfrac{\mathrm{d}\omega_t}{\mathrm{d}t} = T_m - T_{sh} \\ 2H_g \dfrac{\mathrm{d}\omega_g}{\mathrm{d}t} = T_{sh} - T_e \\ \dfrac{\mathrm{d}\theta_{sh}}{\mathrm{d}t} = \omega_{eb}(\omega_t - \omega_g) \\ T_{sh} = K_{sh}\theta_{sh} + D_{sh}(\omega_t - \omega_g) \end{cases} \tag{3}$$

where H_t and H_g are the inertial time constants of WT and PMSG, respectively; ω_t is the WT speed of generator rotor; θ_{sh} is the torsion angle of WT relative to the generator rotor; K_{sh} is the stiffness coefficient of shaft system; D_{sh} is the damping coefficient of shaft system; and T_m, T_e, and T_{sh} are the mechanical, electromagnetic, and shaft system torques, respectively.

C. MSC Model

The active power generated by PMSG P_e is expressed as:

$$P_e = \psi_f i_{sq} \omega_g \tag{4}$$

From (4), T_e and P_e can be accurately controlled by varying i_{sq}. The active power control loop of MSC is shown in Fig. 2.

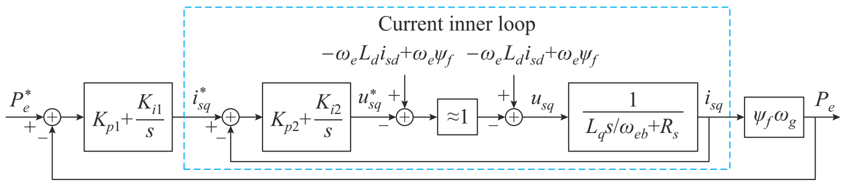

Fig. 2. Active power control loop of MSC.

In Fig. 2, the superscript * represents the reference value; K_{p1} and K_{i1} are the proportional and integral coefficients for the power outer loop of MSC, respectively; and K_{p2} and K_{i2} are the proportional and integral coefficients of the current inner loop on MSC, respectively. P_e^* can be expressed as:

$$P_e^* = \begin{cases} k_{opt}\omega_g^3 & 0 < v < v_r \\ 1 & v_r \le v < v_{\max} \end{cases} \tag{5}$$

where k_{opt} is the MPPT curve coefficient; and v, v_r, and $v_{\max}$ are the actual, rated, and maximum wind speeds, respectively.

Based on Fig. 2, the variable transfer of the active power control loop can be formulated as [22]:

$$\begin{cases} i_{sq}^* = (P_e^* - P_e)\left(K_{p1} + \dfrac{K_{i1}}{s}\right) \\ u_{sq} = -(i_{sq}^* - i_{sq})\left(K_{p2} + \dfrac{K_{i2}}{s}\right) \\ i_{sq} = -\dfrac{u_{sq}}{L_q s/\omega_{eb} + R_s} \end{cases} \tag{6}$$

III. Torsional Oscillation Damping Characteristics

This section presents the effect of electromagnetic torque T_e on the torsional oscillation damping characteristics during MPPT. We derive the incremental transfer function of the electromagnetic torque and rotational speed difference, calculate the quantitative expression of electrical damping based on the electrical damping of synchronous generators (SGs), and analyze the effect of electrical damping on shaft system damping. Our findings provide a foundation for analyzing the influence of the PMSG parameters on the shaft system damping characteristics.

A. Electrical Damping Characteristics of PMSG

Using electromagnetic damping analysis, the linearized electromagnetic torque of PMSG ΔT_e can be expressed as:

$$\Delta T_e = D_e \Delta\omega_\Delta + K_e \Delta\theta_{sh} \tag{7}$$

where D_e and K_e are the electrical damping and synchronization coefficients of the PMSG, respectively; and $\Delta\omega_\Delta$ is the difference between $\Delta\omega_g$ and $\Delta\omega_t$, i.e., $\Delta\omega_\Delta = \Delta\omega_t - \Delta\omega_g$.

We omit self-damping and the generator rotor. Using (3) and (7), the transfer function for torsional angle θ_{sh} and mechanical torque T_m is given by:

$$\frac{\Delta\theta_{sh}}{\Delta T_m} = \frac{\dfrac{\omega_{eb}}{2H_t}}{s^2 + \left(\dfrac{D_{sh}}{2H_t} + \dfrac{D_{sh}}{2H_g} - \dfrac{D_e}{2H_g}\right)s + \omega_{eb}\left(\dfrac{K_{sh}}{2H_t} + \dfrac{K_{sh}}{2H_g} - \dfrac{K_e}{2H_g}\right)} \tag{8}$$

The damping attenuation factor for torsional oscillation ξ can be determined using (8) as:

$$\xi = \frac{D_{sh}(H_t + H_g) - D_e H_t}{4H_t H_g \omega_{osc}} \tag{9}$$

where ω_{osc} is the natural oscillation angular frequency of the shaft system, and $\omega_{osc} = \sqrt{\omega_{eb}[K_{sh}/(2H_t) + (K_{sh} - K_e)/(2H_g)]}$.

The electrical damping coefficient D_e has a negative correlation with the torsional oscillation damping coefficient ξ. When $D_e < 0$, the phase difference between ΔT_e and $\Delta\omega_\Delta$ lies in $(90°, 270°)$, resulting in an increase in ξ. This in turn leads to a positive damping of the shaft system, enhancing its stability. When $D_e > 0$, the phase difference between ΔT_e and $\Delta\omega_\Delta$ falls in $(0, 90°)$, causing ξ to decrease. Consequently, the shaft system experiences negative damping and thus instability.

B. Shaft System Damping Characteristics of PMSG

To obtain the small-signal output power of the PMSG, the MPPT curve can be approximated by a linear function around the steady-state operating point as:

$$\Delta P_e^* = 3k_{opt}\omega_{g0}^2 \Delta\omega_g \tag{10}$$

where ΔP_e^* is the linearized increment of the reference generator output power; $\Delta\omega_g$ is the linearized increment of the generator speed; and ω_{g0} is the generator speed at the stable running point.

The linearized increment of reference electromagnetic torque on the MPPT curve can be formulated as:

$$\Delta T_e^* = 2k_{opt}\omega_{g0}\Delta\omega_g \tag{11}$$

By combining (2) and (4)-(6), the electromagnetic torque can be expressed as:

$$T_e = \psi_f i_{sq} = \psi_f \frac{k_{opt} n_1 n_2 \omega_g^3 - n_1 n_2 T_e \omega_g}{R_s + L_q s/\omega_{eb} + n_2} \tag{12}$$

where $n_1 = K_{p1} + K_{i1}/s$; and $n_2 = K_{p2} + K_{i2}/s$.

Linearizing both sides of the equation simultaneously allows to formulate the incremental transfer function for the linearized electromagnetic torque ΔT_e and $\Delta\omega_\Delta$ as (13).

$$\frac{\Delta T_e}{\Delta\omega_\Delta} = -\psi_f \frac{H_t}{H_t + H_g} \frac{2k_{opt}\omega_{g0}^2 [K_{p1}K_{p2}s^2 +}{L_q s^3/\omega_{eb} + (R_s + K_{p2} + \omega_{g0}\psi_f K_{p1}K_{p2})s^2 +} \rightarrow$$
$$\leftarrow \frac{(K_{p1}K_{i2} + K_{i1}K_{p2})s + K_{i1}K_{i2}]}{[K_{i2} + \omega_{g0}\psi_f (K_{p1}K_{i2} + K_{i1}K_{p2})]s + \omega_{g0}\psi_f K_{i1}K_{i2}} \tag{13}$$

Further, considering (13), we have (14).

$$\begin{cases} m = 2k_{opt}\omega_{g0}^2 \dfrac{H_t}{H_t + H_g} \\ G(s) = -\psi_f \dfrac{K_{p1}K_{p2}s^2 + (K_{p1}K_{i2} + K_{i1}K_{p2})s +}{L_q s^3/\omega_{eb} + (R_s + K_{p2} + \omega_{g0}\psi_f K_{p1}K_{p2})s^2 +} \rightarrow \\ \quad \leftarrow \dfrac{K_{i1}K_{i2}}{[K_{i2} + \omega_{g0}\psi_f (K_{p1}K_{i2} + K_{i1}K_{p2})]s + \omega_{g0}\psi_f K_{i1}K_{i2}} \end{cases} \tag{14}$$

The derivation process is detailed in Supplementary Material A.

The linearized electromagnetic torque can be expressed as $\Delta T_e = mG(s)\Delta\omega_\Delta$.

According to (7) and (13), the real part of the incremental transfer function for ΔT_e and $\Delta\omega_\Delta$ corresponds to the electrical damping coefficient D_e. Moreover, as indicated by (9), D_e is the sole controllable parameter influencing shaft system damping. Hence, investigating the impact of system parameters on D_e is essential for enhancing the damping.

IV. Influence of System Parameters on Torsional Oscillation Damping Characteristics

In this section, we examine the correlation between D_e and various system parameters: ω_{g0}, R_s, K_{p1}, K_{i1}, K_{p2}, K_{i2}, and v. Specifically, we investigate the effects of wind speed v, the PMSG parameters, and control parameters on D_e and the oscillation characteristics of shaft system. Accordingly, we establish a theoretical basis for the proposed torsional oscillation suppression strategy outlined in Section V.

The main parameters of the PMSG-based wind generation system provided by China Wind Power Group Limited are listed in Table I. In addition, the control parameters are tuned using Simulink to achieve the optimal performance.

A. Influence of Wind Speed and Stator Resistance on D_e

Figure 3 shows the Bode diagram of $\Delta T_e/\Delta\omega_\Delta$ with various ω_{g0} ranging from 0.6 to 1.0 p.u., where θ_{osc} is the phase angle of transfer function $G(s)$ at ω_{soc}. The phase lag of ΔT_e with respect to $\Delta\omega_\Delta$ falls between 90° and 180° near ω_{osc}.

TABLE I
Main Parameters of PMSG-based Wind Generation System

Parameter	Value
Base power value S_b	2 MW
Base value of AC phase voltage U_b	575 V
Base value of DC-link voltage U_{dcb}	1150 V
Base value of stator angular frequency ω_{eb}	377 rad/s
Base value of PMSG rotor speed ω_{mb}	7.85 rad/s
Base value of grid angular frequency ω_b	377 rad/s
Rated frequency of PMSG f_n	60 Hz
Pole pair of PMSG n_p	48
Magnetic flux linkage of PMSG rotor ψ_f	1.18842 p.u.
d-axis self-inductance of PMSG stator L_d	0.5131 p.u.
q-axis self-inductance of PMSG stator L_q	0.5131 p.u.
Stator resistance of PMSG R_s	0.0001 p.u.
Inertia time constant of WT H_t	6.69 s
Inertia time constant of PMSG H_g	1 s
Damping coefficient of shaft system D_{sh}	1 p.u.
Stiffness coefficient of shaft system K_{sh}	1.6 p.u.
Proportional coefficient of power outer loop on MSC K_{p1}	1 p.u.
Integral coefficient of power outer loop on MSC K_{i1}	20 s^{-1}
Proportional coefficient of current inner loop on MSC K_{p2}	1 p.u.
Integral coefficient of current inner loop on MSC K_{i2}	10 s^{-1}
Capacitance of DC-link voltage C	0.6232 p.u.
Proportional coefficient of voltage outer loop on GSC K_{p3}	5 p.u.
Integral coefficient of voltage outer loop on GSC K_{i3}	300 s^{-1}
Proportional coefficient of current inner loop on GSC K_{p4}	0.83 p.u.
Integral coefficient of current inner loop on GSC K_{i4}	5 s^{-1}
Grid inductance L_{cg}	0.55 p.u.
Grid resistance R_{cg}	0.006 p.u.
Lowpass filter for P_e ω_P	100 rad/s
PLL filter ω_f	100 rad/s
Proportional coefficient of PLL $K_{p,pll}$	4.1 p.u
Integral coefficient of PLL $K_{i,pll}$	200 s^{-1}

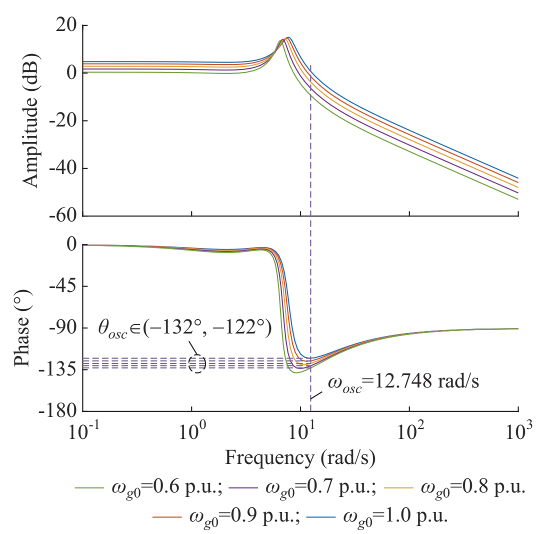

Fig. 3. Bode diagram of $\Delta T_e/\Delta\omega_\Delta$ with various ω_{g0}.

Hence, D_e is negative, resulting in positive damping provided by ΔT_e for the shaft system, thus improving the system stability. The D_e values corresponding to various ω_{g0} are presented in Table II. D_e decreases as ω_{g0} increases, indicating an enhanced effect of the electromagnetic torque on the shaft system damping.

TABLE II
D_e VALUES CORRESPONDING TO VARIOUS ω_{g0}

ω_{g0} (p.u.)	D_e
0.6	−0.248
0.7	−0.334
0.8	−0.428
0.9	−0.527
1.0	−0.626

The variation range of the stator resistance should be moderated when investigating the impact of temperature changes on R_s. The Bode diagram of $\Delta T_e/\Delta\omega_\Delta$ and the corresponding D_e are shown in Fig. 4 and Table III, respectively, with various R_s. The curves in the diagram are very similar, suggesting that changes in R_s have a small influence on D_e. Thus, the effect of ΔT_e on the shaft system damping is negligible and does not affect the stability of the shaft system under MPPT.

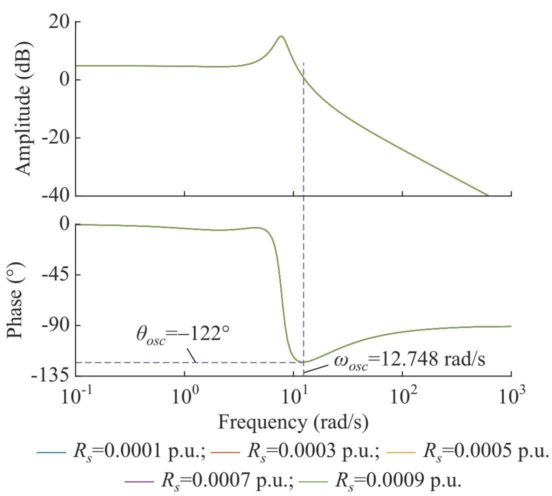

Fig. 4. Bode diagram of $\Delta T_e/\Delta\omega_\Delta$ with various R_s.

TABLE III
D_e VALUES CORRESPONDING TO VARIOUS R_s

R_s (p.u.)	D_e (p.u.)
0.0001	−0.6260
0.0003	−0.6260
0.0005	−0.6260
0.0007	−0.6260
0.0009	−0.6259

B. Influence of Control System Parameters on D_e

The active power control loop comprises two PI controllers and four control parameters: K_{p1}, K_{i1}, K_{p2}, and K_{i2}. We set $K_{p1}=1$ p.u., $K_{i1}=20\ \text{s}^{-1}$, $K_{p2}=1$ p.u., and $K_{i2}=10\ \text{s}^{-1}$ as default control parameters. Subsequently, we select parameter within the ranges of 1-3 p.u. for K_{p1}, 5-25 s^{-1} for K_{i1}, 1-3 p.u. for K_{p2}, and 10-30 s^{-1} for K_{i2}.

Using (13), the Bode diagram of $\Delta T_e/\Delta\omega_\Delta$ with various K_{p1} ranging from 1 to 3 p.u. is shown in Fig. 5. The phase lag of ΔT_e with respect to $\Delta\omega_\Delta$ falls between 90° and 180° near ω_{osc} for K_{p1} of 1.0, 1.5, 2.0, 2.5, and 3.0 p.u.. In such cases, D_e is negative, indicating that T_e contributes to positive damping of the shaft system, thus enhancing its stability. When $K_{p1}=3.0$ p.u., the phase lag of T_e with respect to $\Delta\omega_\Delta$ is between 0° and 90° near ω_{osc}. In this case, the negative value of D_e suggests that T_e still contributes to positive damping of the shaft system, but its stability deteriorates. Table IV lists the D_e values corresponding to various K_{p1}. As the PMSG operates under the MPPT, D_e transitions from negative to positive as K_{p1} increases. This indicates a weakening effect of the electromagnetic torque on the shaft system damping, which is unfavorable to stability.

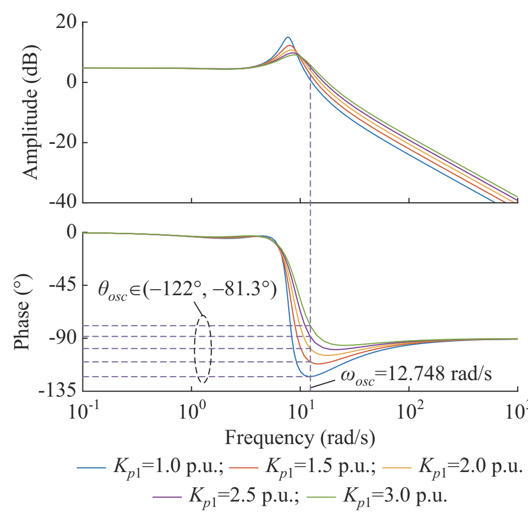

Fig. 5. Bode diagram of $\Delta T_e/\Delta\omega_\Delta$ with various K_{p1}.

TABLE IV
D_e VALUES CORRESPONDING TO VARIOUS K_{p1}

K_{p1} (p.u.)	D_e (p.u.)
1.0	−0.63
1.5	−0.51
2.0	−0.30
2.5	0.01
3.0	0.31

We also use (13) to obtain the Bode diagram of $\Delta T_e/\Delta\omega_\Delta$ with various K_{i1} ranging from 5 to 25 s^{-1} in steady states. As shown in Fig. 6, for K_{i1} of 5, 10, 15, 20, and 25 s^{-1}, the phase lag of ΔT_e with respect to $\Delta\omega_\Delta$ falls between 90° and 180° near ω_{osc}. In such cases, D_e is negative, indicating that T_e contributes to the positive damping of shaft systems, thereby enhancing its stability. The D_e values corresponding to various K_{i1} are listed in Table V. When the PMSG operates under the MPPT, D_e decreases as K_{i1} increases, thereby augmenting the damping effect of the electromagnetic torque on the shaft system and improving its stability.

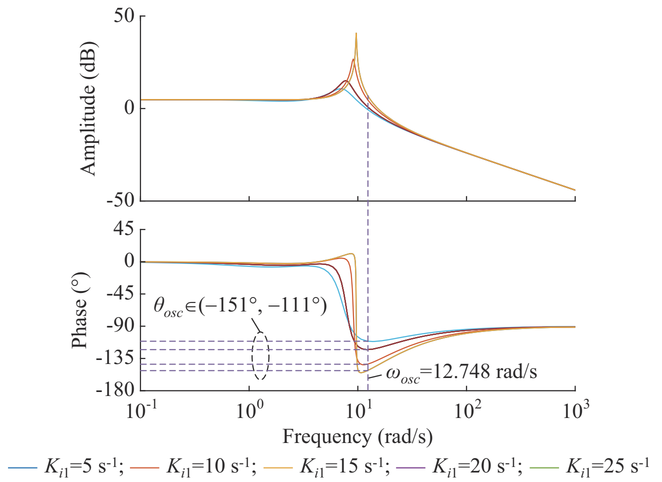

Fig. 6. Bode diagram of $\Delta T_e/\Delta\omega_\Delta$ with K_{i1}.

TABLE V
D_e VALUES CORRESPONDING TO VARIOUS K_{i1}

K_{i1} (s^{-1})	D_e (p.u.)
5	−0.36
10	−0.63
15	−0.96
20	−1.37
25	−1.91

The analysis regarding K_{p2} and K_{i2} and their impacts on the shaft stability is analogous to the analysis conducted for K_{p1} and K_{i1}, respectively, as given in Figs. 7 and 8 and Tables VI and VII, which is thus not discussed further in this subsection.

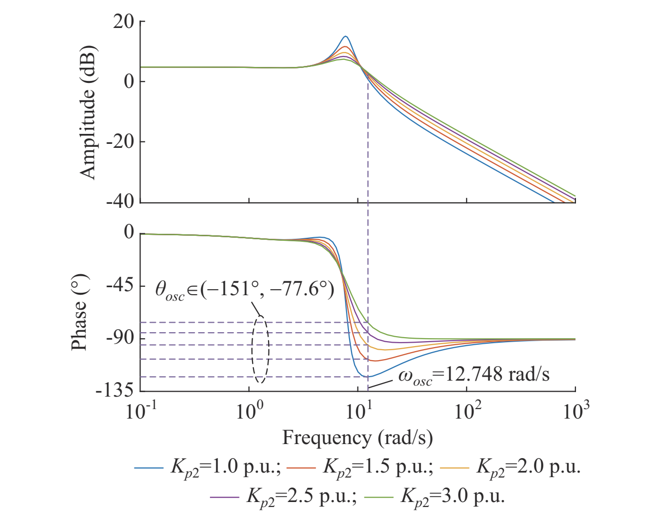

Fig. 7. Bode diagram of $\Delta T_e/\Delta\omega_\Delta$ with K_{p2}.

V. TORSIONAL OSCILLATION SUPPRESSION STRATEGY

We present a system comprising MPPT, MSC, and GSC control strategies. The MSC aims to regulate the output active power P_e and the d-axis stator current.

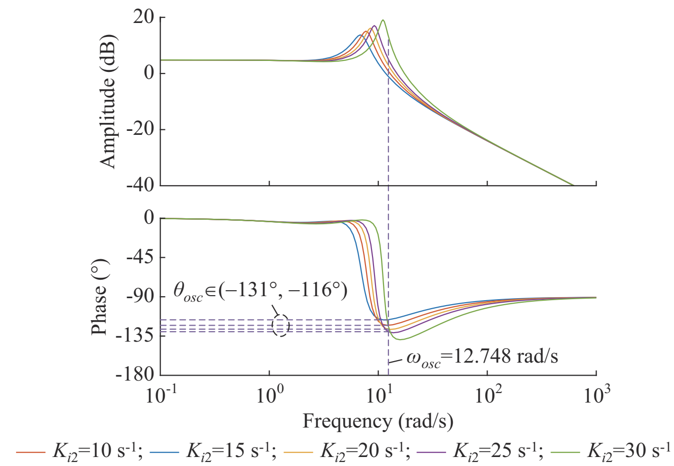

Fig. 8. Bode diagram of $\Delta T_e/\Delta\omega_\Delta$ with various K_{i2}.

TABLE VI
D_e VALUES CORRESPONDING TO VARIOUS K_{p2}

K_{p2} (p.u.)	D_e (p.u.)
1.0	−0.63
1.5	−0.41
2.0	−0.15
2.5	0.10
3.0	0.33

TABLE VII
D_e VALUES CORRESPONDING TO VARIOUS K_{i2}

K_{i2} (s^{-1})	D_e (p.u.)
10	−0.41
15	−0.63
20	−0.88
25	−1.20
30	−1.61

An additional damping controller is introduced into the active power control loop to mitigate torsional oscillations in a PMSG-based wind generation system.

A. Proposed Torsional Oscillation Suppression Strategy

To enhance the effect of the electromagnetic torque on the shaft system damping, D_e should be reduced, as discussed in Section IV. Therefore, we introduce an additional damping controller into the active power control loop. Figure 9 shows the linearized model of the transfer relationship between ΔT_m and $\Delta\omega_\Delta$, which is obtained using (1) and (13). The dotted line in Fig. 9 represents the addition of damping controller $H(s)$. The transitive relation between ΔT_e and $\Delta\omega_\Delta$ can be derived as:

$$\begin{aligned}\Delta T_e &= (m+H(s))G(s)\Delta\omega_\Delta = (m+H(\mathrm{j}\omega))G(\mathrm{j}\omega)\Delta\omega_\Delta = \\ &m\left|G(\mathrm{j}\omega)\right|\mathrm{e}^{\mathrm{j}\theta}\Delta\omega_\Delta + \left|H(\mathrm{j}\omega)\right|\left|G(\mathrm{j}\omega)\right|\mathrm{e}^{\mathrm{j}\theta+\varphi}\Delta\omega_\Delta \end{aligned} \tag{15}$$

where θ is the phase angle of transfer function $G(s)$; and φ is the phase angle of transfer function $H(s)$.

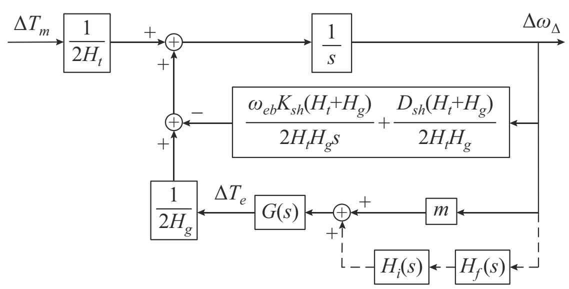

Fig. 9. Linearized model of transfer relationship between ΔT_m and $\Delta\omega_\Delta$.

With the additional damping controller in the active power control loop, D_e near ω_{osc} can be expressed as:

$$\begin{cases} D_e = D_{e0} + D_{eH} \\ D_{e0} = m \cdot \mathrm{Re}(|G(\mathrm{j}\omega_{osc})| \mathrm{e}^{\mathrm{j}\theta_{osc}}) \\ D_{eH} = \mathrm{Re}(|H(\mathrm{j}\omega_{osc})||G(\mathrm{j}\omega_{osc})| \mathrm{e}^{\mathrm{j}\varphi_{osc}}) \end{cases} \tag{16}$$

where D_{e0} is the electrical damping coefficient without the additional damping controller; D_{eH} is the additional electrical damping coefficient with the additional damping controller; and φ_{osc} is the phase angle of transfer function $H(s)$ at ω_{osc}.

From (16) and the expression of $G(s)$, the system reaches stability, with both the amplitude and phase of $G(s)$ remaining stable once the operating conditions, control parameters, and system parameters are determined. Therefore, based on $G(s)$, we can adjust the amplitude and phase of $|H(\mathrm{j}\omega_{osc})|$ to compensate for phase φ_{osc} by modifying additional damping controller $H(s)$ and the internal parameters. This adjustment aims to decrease D_e, enhance the damping effect of T_e on the shaft system, and improve the stability of the shaft system.

The additional damping controller $H(s)$ comprises two primary components: bandpass filter controller $H_f(s)$ and phase compensation controller $H_i(s)$. The bandpass filter controller $H_f(s)$ employs a second-order bandpass filter expressed as:

$$H_f(s) = \frac{2\xi_f \omega_n s}{s^2 + 2\xi_f \omega_n s + \omega_n^2} \tag{17}$$

where ξ_f is the damping ratio of $H_f(s)$; and ω_n is the center angular frequency of $H_f(s)$.

We set the damping ratio of $H_f(s)$ to be $\xi_f = 0.15$. In addition, the center angular frequency of the bandpass filter, $\omega_n = 12.748$ rad/s, corresponds to the inherent oscillation angular frequency of the shaft system.

The phase compensation controller $H_i(s)$ enhances the controller performance, and its transfer function is given by:

$$H_i(s) = K_{tod}\left(\frac{1+sT_1}{1+sT_2}\right)^2 \tag{18}$$

where K_{tod} is the damping controller gain; and T_1 and T_2 are the lead and lag correction time constants, respectively.

The additional damping controller $H(s)$ is formulated as:

$$H(s) = H_f(s)H_i(s) = K_{tod}\left(\frac{1+sT_1}{1+sT_2}\right)^2 \frac{2\xi_f \omega_n s}{s^2 + 2\xi_f \omega_n s + \omega_n^2} \tag{19}$$

Figure 10 shows a model of a PMSG-based wind farm (WF) connected to a four-machine two-area system. In this model, the WF comprises two PMSG-based wind generation systems with different parameters, which are equivalent to two 350 MW WFs, denoted as WF1 and WF2, respectively [23]. The parameters for the AC grid and SGs are shown in Supplementary Material B and have some modifications. The parameters for the PMSG-based wind generation system of WF1 are listed in Table I, whereas those for WF2 are provided in Supplementary Material C.

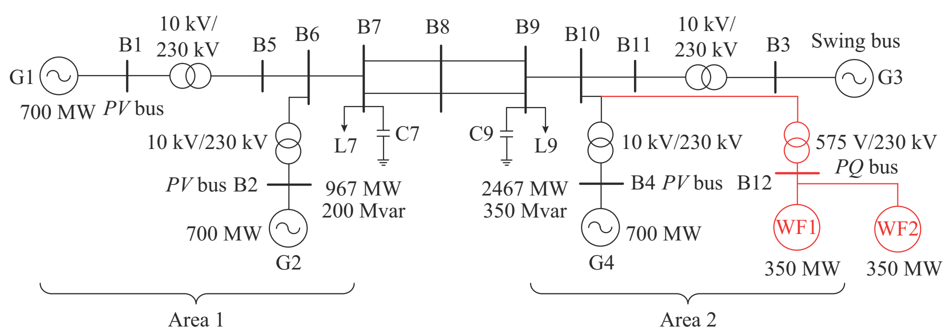

Fig. 10. Model of PMSG-based WF connected to four-machine two-area system.

This model is employed to evaluate the torsional oscillation damping characteristics of PMSG-based wind generation systems with various parameters. We also investigate the independence of the torsional oscillation suppression strategies when multiple PMSG-based wind generation systems with different parameters are connected to power grid. Additionally, the coupling characteristics of the damping controller and torsional oscillation are examined.

Increasing K_{tod} enhances the torsional oscillation suppression ability of the damping controller but introduces a new oscillation mode. Excessive K_{tod} values can lead to positive real roots, thereby impacting the system stability. Therefore, the impact of K_{tod} on the system stability should be analyzed. Supplementary Material D presents a detailed linearization model of a PMSG-based WF connected to the four-machine two-area system.

The main oscillations are categorized into eight modes (modes 1-8): ① local oscillation mode dominated by the SGs in area 1; ② local oscillation mode dominated by the SGs in area 2; ③ torsional oscillation mode dominated by shaft system of WF1; ④ oscillation mode dominated by the PLL; ⑤ interarea oscillation mode dominated by all the SGs; ⑥ oscillation mode dominated by the proposed additional damping controller in WF1; ⑦ torsional oscillation mode dominated by shaft system of WF2; and ⑧ oscillation mode dominated by the proposed additional damping controller in WF2.

First, we vary K_{tod1} from 0 to 24 with an increment step of 0.08. The root loci of oscillation modes are shown in Fig. 11(a). As shown in Fig. 11(b), when K_{tod1} increases, modes 3 and 6 initially converge and then gradually diverge. The absolute value for the damping ratio of mode 3 first increases and then decreases, and when K_{tod1} reaches 0.48, it reaches the maximum value. Additionally, the variation in K_{tod1} has no effect on modes 7 and 8. Concurrently, we increase K_{tod2} from 0 to 24 with an increment step of 0.08. As shown in Fig. 12, with an increase in K_{tod2}, the root loci of modes 7 and 8 follow the same trend as those of modes 3 and 6 when K_{tod1} increases, respectively. Furthermore, the changes in the damping characteristics of shaft system for WF2 do not affect those for WF1. Therefore, when dealing with multiple WTs connected to AC power systems, a shaft system damping controller should be designed considering the characteristics of each PMSG-based wind generation system.

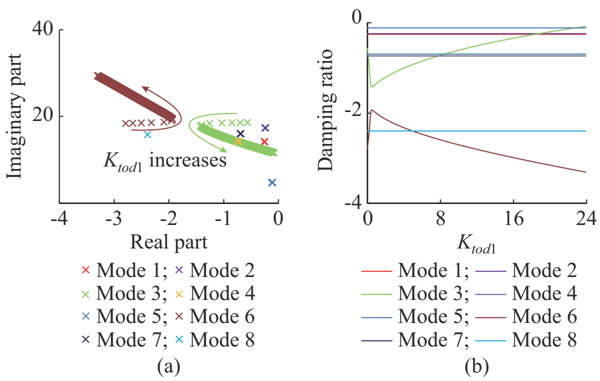

Fig. 11. Root loci and damping ratio of oscillation modes 1-8 with various K_{tod1}. (a) Root loci. (b) Damping ratio.

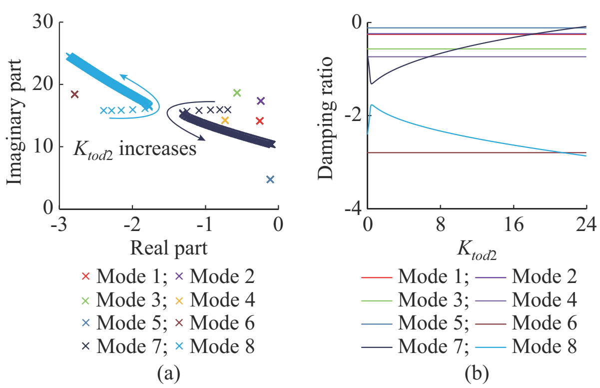

Fig. 12. Root loci and damping ratio of oscillation modes 1-8 with various K_{tod2}. (a) Root loci. (b) Damping ratio.

B. Implementation of Proposed Torsional Oscillation Suppression Strategy

The proposed oscillation suppression strategy is summarized in the following steps.

Step 1: determine the system operating and control parameters such as wind speed, inertial time constants, stator resistance, K_{p1}, K_{i1}, K_{p2}, and K_{i2}.

Step 2: calculate the torsional oscillation frequency.

Step 3: obtain the Bode diagram of $\Delta T_e/\Delta\omega_\Delta$ using (13).

Step 4: calculate the phase angle of the Bode diagram at the torsional oscillation frequency and obtain the compensation angle.

Step 5: calculate the parameters of the phase compensation and bandpass filter controllers based on the compensation angle.

Step 6: obtain the optimal damper controller gain K_{tod} based on eigenvalue analysis.

Based on the parameters listed in Table I, when the system reaches steady state, the phase-frequency characteristics of $G(s)$ are depicted in Fig. 13 with various ω_{g0} ranging from 0.7 to 1.1 p.u.. Figure 13 shows that θ_{osc} ranges from $-132°$ to $-122°$ at ω_{osc} of 12.748 rad/s. For instance, taking ω_{g0}=1.1 p.u. as a reference, the phase angle at ω_{osc} in the shaft system stabilizes at approximately $-122°$ during steady-state operation.

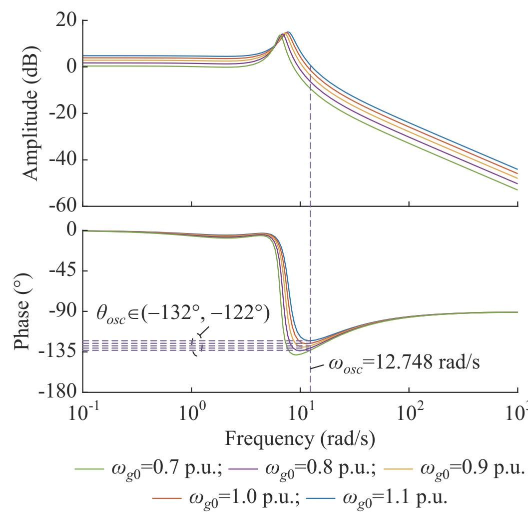

Fig. 13. Phase-frequency characteristic of $G(s)$ with various ω_{g0}.

Based on (9) and (13), when ΔT_e and $\Delta\omega_\Delta$ are in antiphase, D_e reaches its minimum value, and the damping provided by ΔT_e is maximized, considerably benefiting the shafting stability. Hence, $H(s)$ is used to adjust the phase angle of $G(s)$ at ω_{osc} to $-180°$. The phase angle that $H_i(s)$ must compensate is $\varphi_{osc}=-130°-\theta_{osc}=-53°$. Time constants T_1 and T_2 are computed as 0.56 and 0.2 s, respectively. The phase-frequency characteristic of $G(s)$ after incorporating $H(s)$ is shown in Fig. 14. By comparing Figs. 13 and 14, the phase angle of $G(s)$ at ω_{osc} has been adjusted to $-180°$, maximizing the damping effect of ΔT_e.

VI. Case Study

We conduct simulations using the MATLAB/Simulink platform to evaluate the effectiveness of the proposed torsional oscillation suppression strategy. The simulations are executed on a personal computer equipped with a 3.3 GHz processor and 16 GB of RAM to implement the model depicted in Fig. 1. The converter is modeled as a digital system with a switching frequency of 2 kHz and sampling time of 5×10^{-6} s.

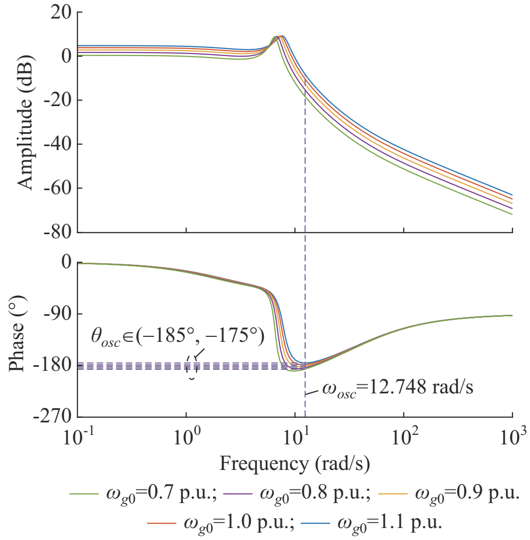

Fig. 14. Phase-frequency characteristic of $G(s)$ with various ω_{g0} after incorporating $H(s)$.

The parameters of the PMSG-based wind generation system listed in Table I are obtained from China Wind Power Group Limited based on an actual system. In addition, the control parameters are fine-tuned using Simulink to achieve optimal performance.

A. Evaluation of Proposed Torsional Oscillation Suppression Strategy

Throughout the simulation, the wind speed is maintained constant at 12.1 m/s, which corresponds to the rated wind speed. The time-domain simulation incorporates a three-phase short-circuit fault on node B12 of the studied system at $t=50$ s. The fault persists for 0.2 s before being cleared at $t=50.2$ s, after which the system returns to steady state.

The time-domain simulation is aimed to investigate two scenarios with and without applying the proposed torsional oscillation suppression strategy, i.e., scenarios 1 and 2, respectively.

The simulation results of studied system in scenarios 1 and 2 are shown in Fig. 15. The application of the double-mass model and proposed torsional oscillation suppression strategy results in a stabilization of ω_g after the short-circuit fault is cleared. In addition, the system attains transient stability, with P_g, U_{dc}, and voltage at PCC U_o returning to steady-state levels, accompanied by oscillations following the disturbance. Implementing the proposed torsional oscillation suppression strategy mitigates transient instability and reduces the likelihood of low-frequency oscillations during the short-circuit fault. Consequently, the oscillations in ω_g, U_{dc}, U_o, and P_g are attenuated, enhancing the dynamic and steady-state operation of the studied system and improving the power grid stability compared with the results without the additional damping controller.

Then, the fundamental parameters affecting the damping of the shaft system, including wind speed, system parameters, and control parameters, are analyzed. The simulation curves of ω_g and P_g with different wind speeds under MPPT are shown in Fig. 16. Figure 17 shows the simulation curves of ω_g and P_g with various R_s under MPPT. Additionally, Fig. 18 illustrates the simulation curves of ω_g and P_g with various K_{p1} and K_{i1} under MPPT. The results for K_{p2} and K_{i2} are ignored because they are similar to those for K_{p1} and K_{i1}, respectively.

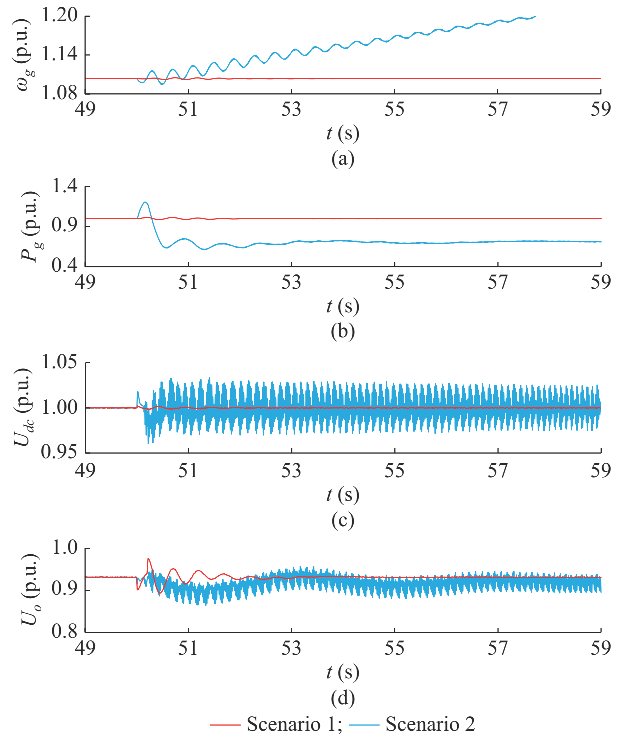

Fig. 15. Simulation results of studied system in scenarios 1 and 2. (a) ω_g. (b) P_g. (c) U_{dc}. (d) U_o.

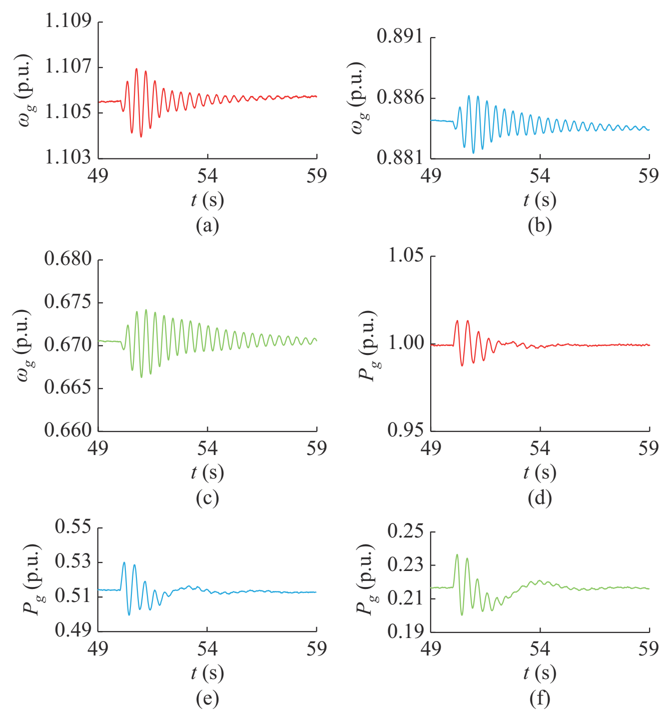

Fig. 16. Simulation curves of ω_g and P_g with different wind speeds under MPPT. (a) ω_g with $v=1.0$ p.u.. (b) ω_g with $v=0.8$ p.u.. (c) ω_g with $v=0.6$ p.u.. (d) P_g with $v=0.8$ p.u.. (e) P_g with $v=1.0$ p.u.. (f) P_g with $v=0.6$ p.u..

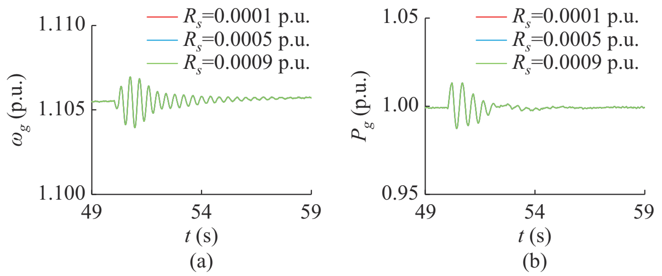

Fig. 17. Simulation curves of ω_g and P_g with various R_s under MPPT. (a) ω_g. (b) P_g.

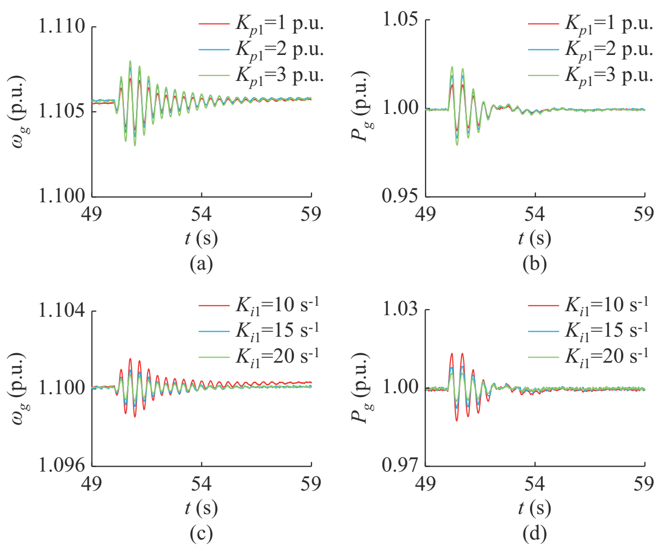

Fig. 18. Simulation curves of ω_g and P_g with various K_{p1} and K_{i1}. (a) ω_g with various K_{p1}. (b) P_g with various K_{p1}. (c) ω_g with various K_{i1}. (d) P_g with various K_{i1}.

Figures 16-18 show that the oscillation amplitudes of ω_g and P_g are smaller and the oscillation attenuation is faster with increase of K_{i1} and K_{i2}, indicating the shaft system damping improves. However, the oscillation amplitude of ω_g and P_g is larger and the oscillation attenuation is slower with increase of K_{p1} and K_{p2}, indicating that the shaft system damping deteriorates. Additionally, the simulation results are nearly insensitive to variations in stator resistance R_s within a reasonable range influenced by temperature.

B. Comparison of Proposed Torsional Oscillation Suppression Strategy with Other Strategies

To evaluate the performance of the proposed torsional oscillation suppression strategy, we compared it with common strategies, including speed-feedback-based damping and active damping based on torque estimation [19].

We consider two cases that illustrate the effectiveness of the proposed torsional oscillation suppression strategy. In case 1, wind speed v remains constant at 12.1 m/s, as in Section VI-A. A three-phase short-circuit fault occurs at node B12 of the system and $t=50$ s in the time-domain simulation. The fault persists for 0.2 s before being cleared at $t=50.2$ s, after which the system returns to steady state. In case 2, the initial wind speed is 12.1 m/s and abruptly drops to 7.3 m/s at $t=50$ s.

Figure 19 shows the transient response curves of ω_g, P_g, U_{dc}, U_o, T_e, and θ_{sh} in response to the three-phase short-circuit fault using the proposed torsional oscillation suppression strategy, active damping strategy considering torque estimation, and damping strategy based on speed feedback [3], [19].

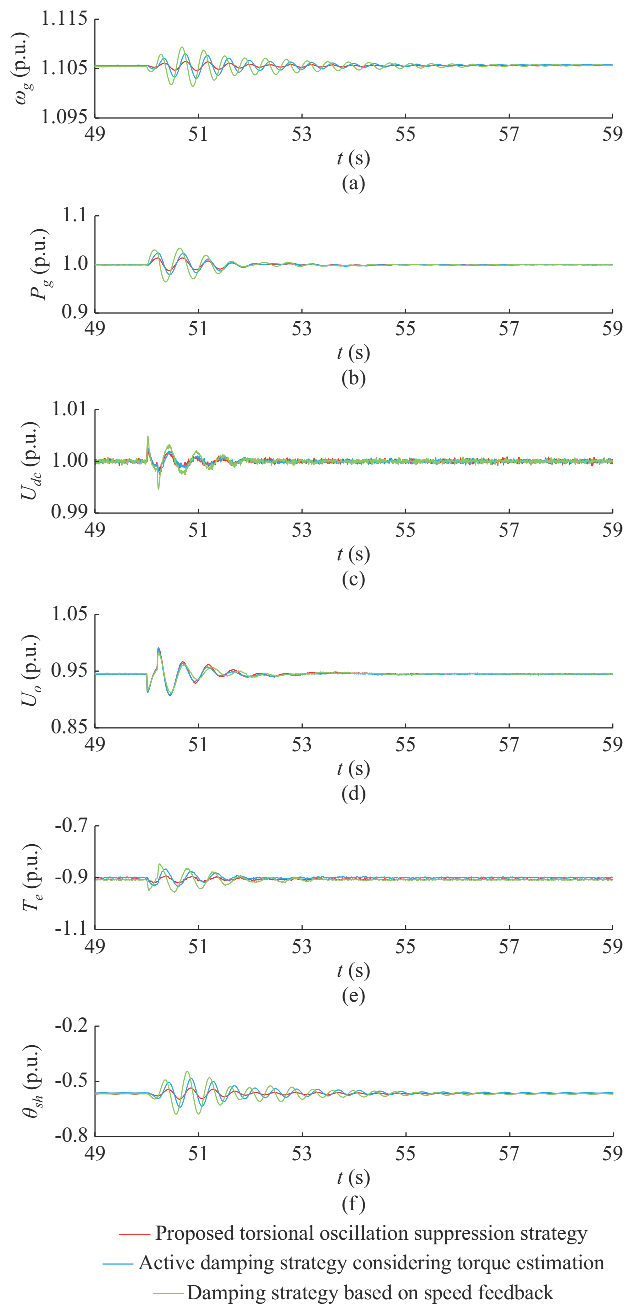

Fig. 19. Transient response curves of ω_g, P_g, U_{dc}, U_o, T_e, and θ_{sh} in response to three-phase short-circuit fault using different control strategies. (a) ω_g. (b) P_g. (c) U_{dc}. (d) U_o. (e) T_e. (f) θ_{sh}.

The proposed torsional oscillation suppression strategy and other strategies improve the shaft system damping and suppress the oscillatory instability of the PMSG-based wind generation system during the three-phase short-circuit fault. The proposed torsional oscillation suppression strategy is more effective in suppressing torsional oscillations than the comparison strategies. Additionally, the proposed torsional oscillation suppression strategy attenuates the oscillations of ω_g, P_g, U_{dc}, T_e, and θ_{sh} faster than other strategies. These results indicate that the proposed torsional oscillation suppression strategy outperforms other strategies in suppressing torsional oscillations.

Figure 20 shows that following a drop in wind speed, P_g, T_e, and ω_g initially decrease, and then stabilize after oscillation attenuation.

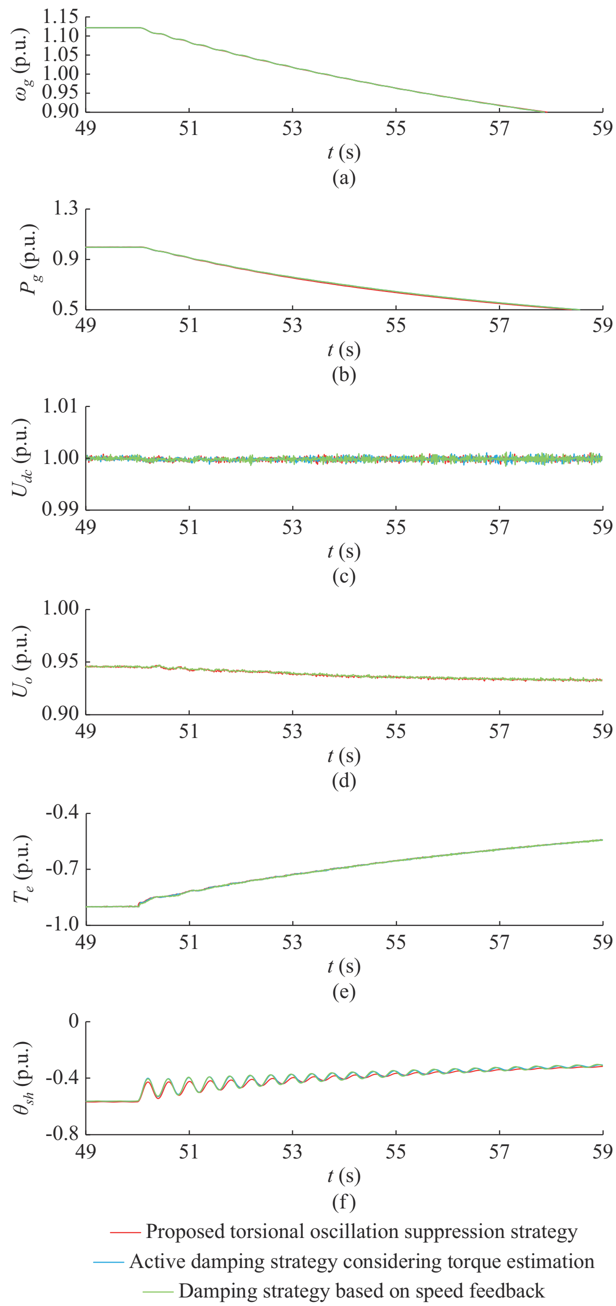

Fig. 20. Transient response curves of ω_g, P_g, U_{dc}, U_o, T_e, and θ_{sh} following a drop in wind speed. (a) ω_g. (b) P_g. (c) U_{dc}. (d) U_o. (e) T_e. (f) θ_{sh}.

Likewise, U_{dc}, θ_{sh}, and U_o oscillate before reaching steady state. The proposed torsional oscillation suppression strategy demonstrates a superior performance in attenuating the oscillations of ω_g, θ_{sh}, and P_g more rapidly compared with other strategies. This superiority is evident in Fig. 20(f), where the oscillation of θ_{sh} is promptly suppressed. The simulation results validate the superiority of the proposed torsional oscillation suppression strategy in suppressing torsional oscillations.

C. Verification of Effect of K_{tod} on System Stability

In this subsection, we analyze the influence of K_{tod} on the system stability. Figure 21 shows the transient response curves of ω_g, P_g, U_{dc}, T_e, and θ_{sh} with various K_{tod}. Figure 21(a) and (e) shows that ω_g and θ_{sh} decrease while the shaft system damping increases with increasing K_{tod}, reaching its peak when $K_{tod}=0.48$. When K_{tod} increases to 2, the shaft system damping decreases, and the decay rates of ω_g and θ_{sh} decline.

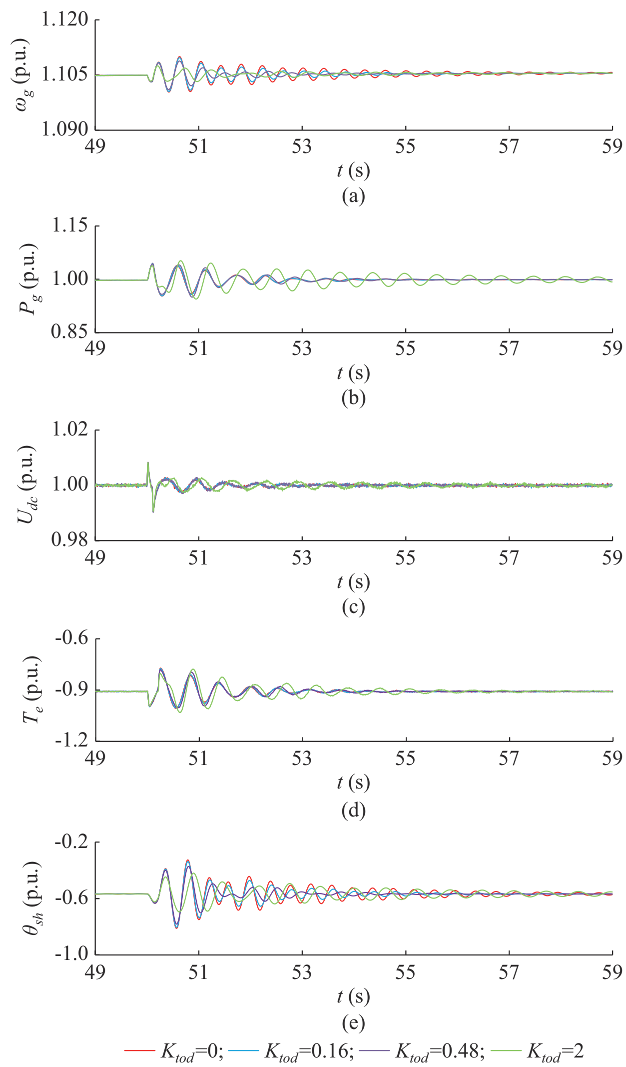

Fig. 21. Transient response curves of ω_g, P_g, U_{dc}, T_e, and θ_{sh} with various K_{tod}. (a) ω_g. (b) P_g. (c) U_{dc}. (d) T_e. (e) θ_{sh}.

In Fig. 21(b)-(d), an increase in K_{tod} results in an increase in the active power reference value, leading to higher oscillation amplitudes in P_g, U_{dc}, and T_e. Therefore, the proper selection of K_{tod} is crucial for effective oscillation suppression. If K_{tod} is excessively small, the suppression effect becomes prominent. By contrast, if K_{tod} is very large, the suppression effect diminishes, increasing the instantaneous values of P_g,

U_{dc}, and T_e, and potentially causing system instability.

VII. Conclusion

We analyze the torsional oscillation damping characteristics based on the electromagnetic damping torque method. Subsequently, the transfer function for electromagnetic torque and speed is derived, and the influence of electromagnetic torque on the shaft system damping is explained.

The electrical damping coefficient D_e is the only controllable parameter that affects the shaft system damping and is negatively correlated with damping coefficient ξ of the torsional oscillation. Additionally, the real part of the incremental transfer function of ΔT_e and $\Delta\omega_\Delta$ is equivalent to electrical damping coefficient D_e.

The influence of wind speed and system control parameters on torsional oscillation damping is determined. We find that v, K_{i1}, and K_{i2} are positively correlated with the shaft system damping, while K_{p1} and K_{p2} are negatively correlated with shaft system damping, and a change in stator resistance R_s within a reasonable range has a negligible effect on damping. Therefore, to ensure the stable operation of a PMSG-based wind generation system, the high-speed operation is recommended. In addition, while ensuring an active power tracking rate and stability in the high-frequency range, we recommend minimizing K_{p1} and K_{p2}, as well as increasing K_{i1} and K_{i2}.

We propose an oscillation suppression strategy on the active power control loop to compensate for the damping angle between ΔT_e and $\Delta\omega_\Delta$ and thus improve the stability of the shaft system based on the previous analysis. The studied system is modeled using MATLAB/Simulink, and the simulation results show that the proposed torsional oscillation suppression strategy outperforms other strategies in eliminating torsional oscillations. The simulation results verifies the effectiveness of our theoretical analysis and control strategy.

In future work, we will investigate an adaptive compensation method for the damping angle of a PMSG-based wind generation system considering the frequency offset.

References

[1] H. Liu and C. Liu, "Frequency regulation of VSC-MTDC system with offshore wind farms," *Journal of Modern Power Systems and Clean Energy*, vol. 12, no. 1, pp. 275-286, Jan. 2024.

[2] B. Sahu and B. P. Padhy, "Design of power system stabilizer for DFIG-based wind energy integrated power systems under combined influence of PLL and virtual inertia controller," *Journal of Modern Power Systems and Clean Energy*, vol. 12, no. 2, pp. 524-534, Mar. 2024.

[3] A. Beiki and M. Rahimi, "An efficient sensorless approach for energy conversion enhancement and damping response improvement in permanent magnet synchronous generator (PMSG) based wind turbines," *International Transactions on Electrical Energy Systems*, vol. 29, no. 1, pp. 18-35, Jan. 2019.

[4] K. A. Singh, A. Chaudhary, and K. Chaudhary, "Three-phase AC-DC converter for direct-drive PMSG-based wind energy conversion system," *Journal of Modern Power Systems and Clean Energy*, vol. 11, no. 2, pp. 589-598, Mar. 2023.

[5] J. Tan and Y. Zhang, "Coordinated control strategy of a battery energy storage system to support a wind power plant providing multi-timescale frequency ancillary services," *IEEE Transactions on Sustainable Energy*, vol. 8, no. 3, pp. 1140-1153, Jul. 2017.

[6] C. Zhang, Z. Li, Q. Gao *et al*., "Damping effects on torsional oscillation of DFIG drive-chain using different control strategies," *Proceedings of the CSEE*, vol. 33, no. 27, pp. 135-144, Sept. 2013.

[7] M. Nasiri and R. Mohammadi, "Peak current limitation for grid side inverter by limited active power in PMSG-based wind turbines during different grid faults," *IEEE Transactions on Sustainable Energy*, vol. 8, no. 1, pp. 3-12, Jan. 2017.

[8] H. Geng, D.-W. Xu, B. Wu *et al*., "Control and Stability analysis for the permanent magnetic synchronous generator based direct driven variable speed wind energy conversion system," *Proceedings of the CSEE*, vol. 29, no. 33, pp. 68-75, Nov. 2009.

[9] G. Wang, Q. Shi, L. Fu *et al*., "Mechanism analysis of torsional vibration for directly-driven wind turbine with permanent magnet synchronous generator shaft system with virtual inertia control," *Electric Machines and Control*, vol. 18, no. 8, pp. 8-16, Aug. 2014.

[10] L. Chen, X. Du, B. Hu *et al*., "Drivetrain oscillation analysis of grid forming type-IV wind turbine," *IEEE Transactions on Energy Conversion*, vol. 37, no. 4, pp. 2321-2337, Dec. 2022.

[11] Z. Hao and Y. Yu, "Torque analysis for the influence of DFIG-based wind farm on damping of power system," *Transactions of China Electrotechnical Society*, vol. 26, no. 5, pp. 152-158, Oct. 2011.

[12] A. J. G. Westlake, J. R. Bumby, and E. Spooner, "Damping the power-angle oscillations of a permanent-magnet synchronous generator with particular reference to wind turbine applications," *IEE Proceedings-Electric Power Applications*, vol. 143, no. 3, pp. 269-280, May 1996.

[13] A. H. Rajaei, M. Mohamadian, S. M. Dehghan *et al*., "PMSG-based variable speed wind energy conversion system using Vienna rectifier," *European Transactions on Electrical Power*, vol. 21, no. 1, pp. 954-972, Jan. 2011.

[14] J. Yao, X. Zeng, and J. Li, "Shaft oscillation characteristics of grid-connected doubly-fed induction generator-based wind power generation system," *Transactions of China Electrotechnical Society*, vol. 32, no. 6, pp. 123-135, Jun. 2017.

[15] L. Wang, L. Cheng, Y. Sun *et al*., "Damping control of drive-train system of DFIG to compensate phase lag characteristics of electromagnetic torque-generator speed closed loop," *Power System Technology*, vol. 38, no. 12, pp. 3333-3340, Mar. 2014.

[16] Z. Zhang, X. Zhao, L. Fu *et al*., "Stability and dynamic analysis of the pmsg-based WECS with torsional oscillation and power oscillation damping capabilities," *IEEE Transactions on Sustainable Energy*, vol. 13, no. 4, pp. 2196-2210, Oct. 2022.

[17] S. S. H. Yazdi, Y. Shokri-Kalandaragh, and M. Bagheri, "Power system stability improvement considering drive train oscillations of virtual synchronous generator-regulated type-4 wind turbines," *IET Renewable Power Generation*, vol. 17, no. 3, pp. 579-603, Feb. 2023.

[18] O. Alizadeh and A. Yazdani, "A strategy for real power control in a direct-drive PMSG-based wind energy conversion system," *IEEE Transactions on Power Delivery*, vol. 28, no. 3, pp. 1297-1305, Jul. 2013.

[19] M. Rahimi and A. Beiki, "Efficient modification of the control system in PMSG-based wind turbine for improvement of the wind turbine dynamic response and suppression of torsional oscillations," *International Transactions on Electrical Energy Systems*, vol. 28, no. 8, pp. 16, Aug. 2018.

[20] O. Alizadeh and A. Yazdani, "A control strategy for power regulation in a direct-drive WECS with flexible drive-train," *IEEE Transactions on Sustainable Energy*, vol. 5, no. 4, pp. 1156-1165, Oct. 2014.

[21] W. Du, Y. Wang, Y. Wang *et al*., "Analytical examination of oscillatory stability of a grid-connected PMSG wind farm based on the block diagram model," *IEEE Transactions on Power Systems*, vol. 36, no. 6, pp. 5670-5683, Nov. 2021.

[22] F. Zhou, "Drive-train torsional vibration suppression of large scale PMSG-based WECS," *Protection and Control of Modern Power Systems*, vol. 7, no. 1, pp. 1-13, Dec. 2022.

[23] B. Shao, S. Zhao, B. Gao *et al*., "Adequacy of the single-generator equivalent model for stability analysis in wind farms with VSC-HVDC systems," *IEEE Transactions on Energy Conversion*, vol. 36, no. 2, pp. 907-918, Jun. 2021.

Yizhuo Ma received the B.S. degree in water conservancy and hydropower engineering from Northwest A&F University, Yangling, China, in 2019, and the M.E. degree in water conservancy engineering from Huazhong University of Science and Technology, Wuhan, China, in 2021. He is currently pursuing a Ph.D. degree in electrical engineering at Shanghai Jiao Tong University, Shanghai, China. His research interests include power system stability analysis and control considering wind power integration.

Jin Xu received the B.S. degree in electrical engineering from Sichuan University, Chengdu, China, in 2013, and the Ph.D. degree from Shanghai Jiao

Tong University, Shanghai, China, in 2019. He is currently an Assistant Professor at Shanghai Jiao Tong University. His research interests include power system stability analysis, power electronic modeling, and real-time simulation.

Guojie Li received the B. Eng. and M. E. degrees in electrical engineering from Tsinghua University, Beijing, China, in 1989 and 1993, respectively, and the Ph. D. degree in electrical engineering from Nanyang Technological University, Singapore, in 1999. He was an Associate Professor with the Department of Electrical Engineering, Tsinghua University. He is currently a Professor with the Department of Electrical Engineering, Shanghai Jiao Tong University, Shanghai, China. His research interests include power system analysis and control, wind and photovoltaic (PV) power control and integration, and microgrid.

Keyou Wang received the B. S. and M. S. degrees in electrical engineering from Shanghai Jiao Tong University, Shanghai, China, in 2001 and 2004, respectively, and the Ph.D. degree from the Missouri S&T (formerly University of Missouri-Rolla), Springfield, America, in 2008. He is currently a Professor and Vice Department Chair of Electrical Engineering at Shanghai Jiao Tong University. His research interests include power system dynamic and stability, renewable energy integration, and converter dominated power system.